Quantitative 3D comparison of biofilm imaged by X-ray micro-tomography and two-photon laser scanning microscopy

Larue Anne Edith, Pascal Swider, Paul Duru, D. Daviaud, Michel Quintard, Yohan Davit

Quantitative 3D comparison of biofilm imaged by X-ray micro-tomography and two-photon laser scanning microscopy

A.E. LARUE*, P. SWIDER*, P. DURU*, D. DAVIAUD†, M. QUINTARD* & Y. DAVIT*
*Institut de Mécanique des Fluides de Toulouse (IMFT) - Université de Toulouse, CNRS, INPT, UPS, Toulouse, France
†Centre de Physiopathologie de Toulouse Purpan (CPTP) - Université de Toulouse, INSERM, CNRS, UPS, Toulouse, France

Key words. Biofilms, contrast agent, porous media, two-photon microscopy, X-ray micro-tomography, 3D printing.

Summary

Optical imaging techniques for biofilm observation, like laser scanning microscopy, are not applicable when investigating biofilm formation in opaque porous media. X-ray micro-tomography (X-ray CMT) might be an alternative but it finds limitations in similarity of X-ray absorption coefficients for the biofilm and aqueous phases. To overcome this difficulty, barium sulphate was used in Davit *et al.* (2011) to enable high-resolution 3D imaging of biofilm via X-ray CMT. However, this approach lacks comparison with well-established imaging methods, which are known to capture the fine structures of biofilms, as well as uncertainty quantification. Here, we compare two-photon laser scanning microscopy (TPLSM) images of *Pseudomonas Aeruginosa* biofilm grown in glass capillaries against X-ray CMT using an improved protocol where barium sulphate is combined with low-gelling temperature agarose to avoid sedimentation. Calibrated phantoms consisting of mono-dispersed fluorescent and X-ray absorbent beads were used to evaluate the uncertainty associated with our protocol along with three different segmentation techniques, namely hysteresis, watershed and region growing, to determine the bias relative to image binarization. Metrics such as volume, 3D surface area and thickness were measured and comparison of both imaging modalities shows that X-ray CMT of biofilm using our protocol yields an accuracy that is comparable and even better in certain respects than TPLSM, even in a nonporous system that is largely favourable to TPLSM.

Introduction

Bacteria often develop in sessile colonies at the interface between two phases, mostly on solid surfaces, where the microorganisms are embedded in a complex self-secreted polymer matrix (Hall-Stoodley *et al.*, 2004; Lewandowski & Beyenal, 2014). Such colonies, called biofilms, are ubiquitous in the environment (Fierer & Jackson, 2006; Lewandowski & Beyenal, 2014) and provide the nested bacteria with a better resistance to various stresses including predators and biocides (Stewart & Costerton, 2001; Mah & O'Toole, 2001). When developing on a substrate, and specifically in porous media, biofilms can induce significant changes to the medium's transport properties (porosity, permeability) (Cunningham *et al.*, 1991; Rittmann *et al.*, 1999; Thullner & Baveye, 2008) with many implications in engineering, for example bio-filters (Ho *et al.*, 2008), soil remediation (Valls & de Lorenzo, 2002; Singh *et al.*, 2006), microbial enhanced oil recovery (MEOR) (Armstrong & Wildenschild, 2012), CO_2 storage (Mitchell *et al.*, 2009; Morozova *et al.*, 2011) and medical applications like biofilms orthopaedic infections (Stoodley, 2011). A variety of systems have been developed to understand the effect of biofilm accumulation in porous media hydrodynamics and mass transport (Cunningham *et al.*, 1991; Rittmann *et al.*, 1999; Valiei *et al.*, 2012) but the challenge of accessing the structure and distribution of biofilms in a 3D porous structure, at the meso-scale, still remains. We argue that the lack of understanding about the fundamentals of biofilm development in porous media is mostly due to the limits of currently used imaging methods (Vafai, 2010).

Indeed, optical imaging techniques have been used on 2D porous structures and transparent 3D porous media (Yarwood *et al.*, 2002; Leon-Morales *et al.*, 2004; Leis *et al.*, 2005; Kim *et al.*, 2010), but these methods are hindered by the opacity of most 3D porous structures. Although magnetic resonance imaging techniques (Seymour *et al.*, 2004) are advancing, such methods yield anisotropic images and do not currently provide sufficient spatial resolution. Approaches based on X-ray computed micro-tomography (X-ray CMT) (Wildenschild & Sheppard, 2013) are also being explored as this technique enables, in theory, the imaging of large volumes of porous media with sub-micron resolution. However, X-ray absorption coefficients for the biofilm and the surrounding aqueous phase

Correspondence to: A.E. Larue, Yohan Davit, Institut de Mécanique des Fluides de Toulouse (IMFT) - Université de Toulouse, CNRS, INPT, UPS, Toulouse, 31400, France. Tel: +33 5 34 32 28 82; e-mail: anne.larue@imft.fr, yohan.davit@imft.fr

are very similar and therefore contrast agents must be used to differentiate between phases. Contrast agents such as silver-coated micro-spheres (Iltis *et al.*, 2011), 1-chloronaphtalene (Rolland du Roscoat *et al.*, 2014), iron sulphate (Carrel *et al.*, 2017) and barium sulphate (BaSO4) (Davit *et al.*, 2011) have been tested, but currently each of these has drawbacks restricting their application to specific experimental conditions.

Silver-coated micro-spheres map the biofilm surface only, making it cumbersome and inaccurate to perform volume segmentation. 1-chloronaphtalene is an oily solvent which may induce complex two-phase flows in a water-saturated porous medium with a reduced penetration in small pores where capillary pressure is too high. Further, as noted by Carrel *et al.* (2017), it is a powerful biocide that may significantly modify the biofilm structure upon contact with the matrix. $BaSO_4$ has the advantages of being nontoxic and to provide a very good contrast on X-ray laboratory machines (Carrel *et al.*, 2017). Its main drawback is the high viscosity of the suspension, which can damage the biofilm structure upon introduction. The fact that a dilute, and thus less viscous, solution of $BaSO_4$ with water causes important sedimentation of the barium sulphate particles, reduces the applicability of this contrast agent. Carrel *et al.* (2017) used iron sulphate $FeSO_4$ in dilute form that is progressively added to the biofilm during the growth phase. This innovative method for marking the biofilm phase only (the first one to do so) was achieved as the inorganic compound $FeSO_4$ renders the biofilm more visible when imaging with phase contrast, although with very little distinction and therefore the potential for uncertainty in the segmentation process. The need for continuous introduction of $FeSO_4$ during growth further limits imaging to laboratory grown biofilms and makes it impossible to visualize samples collected in the environment or from engineering systems. $FeSO_4$ can only be used in phase contrast which is a less accessible technique than absorption contrast.

Each of the elaborated solutions is adapted to specific experimental conditions, it is therefore quite difficult to compare and classify contrast agents among themselves. In fact, considering the variability of biofilms in porous media samples, whether in terms of physical properties (e.g. size and opacity), micro-organism types and investigation inquiries (e.g. scale of studied phenomenon), the search for a single ideal contrast agent may be vain. Instead, we believe that a way forward is to build a library of contrast agents containing specificities, domains of applicability and uncertainty evaluations for each approach. Developing such a library requires not only to find novel contrast agents and protocols, but also to better characterize the existing ones. In particular, we note that, although all the established approaches may yield significant uncertainty, none of the corresponding studies have attempted to quantify it or to compare the results with a well-known 3D imaging method for biofilm. Davit *et al.* (2011) and Iltis *et al.* (2011) compared qualitatively a radiograph with 2D images obtained by shadowscopy and light microscopy, respectively, but a 3D comparison is still required for a complete quantitative analysis. The limitations of commonly used optical imaging methods for 3D imaging of meso-scopic scale samples and for opaque porous media being the main obstacles of such 3D validation.

In this work, we use glass capillaries as a simplified porous medium model, which allows us to image 3D biofilm structures using both X-ray CMT and optical fluorescence imaging, which is by far the most widespread imaging method in the field. More specifically, two-photon laser scanning microscopy (TPLSM) images of biofilm are compared with X-ray CMT using an improved protocol where barium sulphate is combined with a low-gelling temperature agarose to avoid sedimentation and facilitate transport and manipulation by mechanical stabilization. Direct comparison between the two techniques is made possible by an innovative system involving additive manufacturing, which enables rotating the capillary manually for TPLSM acquisition to gather a maximum amount of information without stopping the flow. Uncertainty associated with image processing and segmentation is evaluated using calibrated phantoms consisting of mono-dispersed fluorescent and X-ray absorbent beads. Three different segmentation techniques, namely hysteresis, region growing and watershed were employed for binarization and measurements of biofilm volume, 3D surface area and maximum thickness were performed. Quantitative comparison of both imaging modalities along with the uncertainty yielded by our protocol is achieved.

Materials and methods

Contrast agent preparation for X-ray CMT

The contrast agent was prepared beforehand of each experiment. It consisted of a mixture of commercially available medical-grade barium sulphate suspension (Micropaque®, Guerbet, France) and Sigma-Aldrich® low-gelling temperature agarose. This low-gelling temperature agarose was specially chosen because it enabled the injection of the contrast agent in liquid form. Indeed, it was introduced in the capillary in fluid phase at 37°C and its polymerization was then induced by cooling down the sample in the range 8–17°C. Once polymerized, the hydro-gel remained solid due to a hysteresis effect for temperatures up to its melting point (∼50°C), which allowed for transportation, facilitated manipulations and permitted imaging using X-ray CMT at room temperature without de-polymerization. The gel solution was prepared at a w/v concentration of 2% by mixing 0.2 g of agarose powder with 10 mL of bacterial culture medium in an Erlenmeyer flask. The mixture was then autoclaved at 121°C to ensure complete dissolution of the gel powder and sterilization of the mixture. After autoclaving, barium sulphate suspension was added to the nonpolymerized gel to achieve a concentration of 50% w/w of the gel solution. Barium sulphate particles were approximately 1 μm in size and are insoluble in water. The

stock product contained 1 g per mL of barium sulphate. The mixture was vortexed and filtered using a vacuum pump with 30 μm nylon filters to remove barium sulphate aggregates. The final concentration of barium sulphate in the contrast agent was approximately 30% by weight, slightly decreased by the filtration procedure.

The viscosity of the contrast agent and pure Micropaque® suspension was assessed using a ThermoFisher® (Massachusetts, USA) 2° cone and plate rheometer at 37°C being the temperature at which it was introduced in the sample. For an identical shear rate, the viscosity of the contrast agent ($\sim 10^{-1}$ Pa.s) was 53% smaller than the viscosity of pure barium sulphate suspension ($\sim 2 \times 10^{-1}$ Pa.s).

Biofilm growth protocol

Pseudomonas Aeruginosa (ATCC 10145) expressing green fluorescent protein (GFP) was used as a model organism for this experiment. *P. Aeruginosa* is a gram-negative, facultatively anaerobe bacterium known for producing strong biofilms (Ma *et al.*, 2009; Lieleg *et al.*, 2011). Cultures were reconstructed from frozen stock in 6 mL of sterile culture media (Nutrient Broth from Sigma-Aldrich®) with 300 μL of Ampicillin solution (concentration of 6 mg/mL) and incubated for 48 h at 37°C in sterile centrifuge tubes. Strict aseptic protocol was followed to ensure that no contamination of the original strain occurred. Cultures were then washed via centrifugation at 3000 rpm for 15 min and re-suspended in 1 mL aliquot of fresh culture medium for immediate inoculation in 5 cm-long square-cross sectional VitroCom® (New Jersey, USA) glass capillaries (inner dimensions 500 μm x 500 μm, wall thickness 100 μm). Inoculated capillaries stood overnight. Custom-designed 3D-printed caps filled with silicone were used to ensure watertightness at the capillary ends. Inoculation and flow were done by piercing the caps with 30G needles mounted on a syringe or luer fittings, respectively. On removal of the needle, the puncture was closed, without intervention, by the silicone, ensuring the sealing of the caps.

The fluidic circuit for biofilm growth was set up as shown in Figure 1. It consisted of a micro-fluidic pressure controller (OB1 0–2 bars Elveflow®, France) pressurizing a reservoir filled with ultra-pure water. The reservoir output flowed through a flow sensor (0.2–5 mL/min Elveflow®) which was used to servo-control the flow rate via a computer and the micro-fluidic pressure controller. This enabled maintaining a fixed flow rate throughout the circuit. A Harvard® (Massachusetts, USA) PHD 2000 syringe pump was used to introduce a concentrated culture medium solution (30 times more than normal concentration) in the circuit. Ultra-pure water and nutrient solution met at the T-junction before the capillary to allow mixing and were separated to prevent biofilm from spreading across the fluidic circuit. Indeed, if the main reservoir was filled with nutrient solution at normal concentration, bacteria would move by chemotaxis and form biofilm upstream until reaching the reservoir, fouling the valves and sensors on its way. The nutrient solution in the syringe pump was prepared at a concentration inhibiting bacterial development which has been determined by preliminary experiments. The fluidic circuit was open and effluent flow from the capillaries was directed to a waste reservoir. We will refer to the capillaries as flow cells in the next paragraphs.

After inoculation, the flow cells were connected to the fluidic circuit and flow rate was set at 800 μL/min, flow rate at which

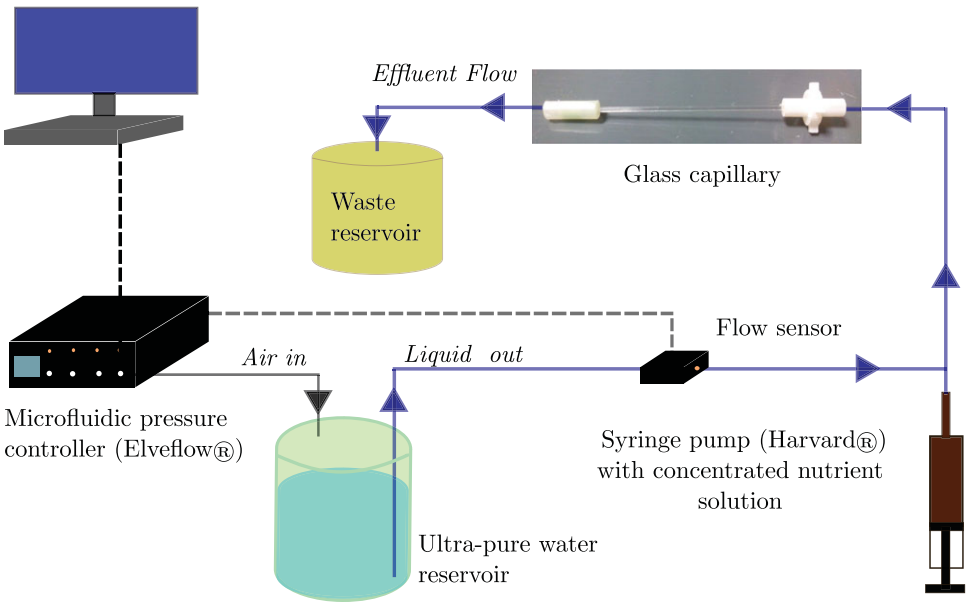

Fig. 1. Fluidic circuit used to grow biofilm for 2 days at fixed flow rate.

biofilm was grown continually for 48 h at room temperature (23.5 $\pm 1^{\circ}$C thermostated room).

Imaging protocol

Two-photon microscopy. This imaging modality was chosen for comparison as it is a widespread technique for biofilm observation (Vroom *et al.*, 1999; Choi *et al.*, 2010; Neu & Lawrence, 2015); it also enables imaging large volumes of hundreds of micrometers to a few millimeters. Approaches based on electron microscopy Sugimoto *et al.* (2016), which are also often used for imaging biofilms, provide a far superior resolution but cannot be used in our case as they are limited in the volume of the sample.

The bacterial strain expressed GFP and a tetramethylrhodamine (TAMRA) conjugate of Concanavalin-A (C80 ThermoFisher® Invitrogen, California, USA) was used to stain polysaccharides (α-mannoprosyl and α-glucopyranosyl residues) from the extracelullar polymeric matrix. The solution was prepared in 0.1 M sodium bicarbonate solution at a concentration of 200 μg/mL of Concanavalin-A. The flow cell was disconnected from the fluidic circuit for the introduction (at approximately 40 μL/min) of the fluorophore, which was then left to stand for 15 min before imaging.

Fluorescence imaging was performed using a (7MP Zeiss®, Germany) two-photon microscope with a 20x immersion lens of numerical aperture 1. Excitation wavelength was 880 nm and GFP from the bacteria appeared in the green channel, whereas the TAMRA attached to the EPS matrix appeared in the red channel. A Z-stack with laser compensation was done over 600 μm of depth until no sufficient signal was perceived. Flow of culture medium was maintained inside the microscope 37°C thermostated cubicle, using a syringe pump, at half the growth flow rate. The flow rate was decreased to prevent potential biofilm detachment which could be caused by the temperature difference from growth conditions.

Due to the refractive index of glass being significantly different from that of water, biofilm grown on the flow cell walls, in the laser direction, was difficult to observe. The custom designed caps and capillary holder, with integrated pool for immersion imaging, illustrated in Figure 2, enabled rotating the capillary at four different angles (0°, 90°, 180° and 270°). This capacity was used for imaging at two different angles (0° and 90°) to gather information on half of the flow cell's cross section. Only two angles were chosen to minimize laser impact on the biofilm structures. Spatial resolution was 1.186 μm/pixel for the focal plane and the Z step between two slices was 1.5 μm. Acquisition time was 20 min for each angle.

X-ray micro-tomography. When fluorescence imaging was complete, the contrast agent for X-ray CMT was immediately introduced. We proceeded to an introduction at a flow rate 10 times less than the growth flow rate as no biofilm sloughing was observed at this flow rate during previous experiments. Once effluent was white due to the barium sulphate, the needles were slowly removed to avoid potential pressure oscillations. The flow cell was refrigerated for 15 min for rapid polymerization of the gel which prevented sedimentation of the barium sulphate particles.

We then proceeded to X-ray CMT image acquisition using a Phoenix Nanotom® (General Electric measurements, France) with a Tungsten target at 90 kV and 80 μA. Low voltage and amperage were selected to prevent excessive heating of the sample and de-polymerizing of the agarose. In addition, lowest scanning time (500 ms per frame) and minimum averaging (3 frames) were selected to reduce total acquisition which was about 1 h and 30 min for images of 2000 $\times$ 2000 pixels of size 2 μm.

Phantom uncertainty measurement

In order to measure the errors generated during every step of image acquisition and processing, an imaging phantom consisting of several fluorescent mono-dispersed beads (Sigma Aldrich®) of diameter 6 $\pm$ 0.18 μm was used. Imaging for both modalities was performed under the same parameter configuration as for the flow cell containing biofilm. For reference values, we used the dimension and confidence interval given by the supplier and bright-field microscopy images as second control.

For evaluation of TPLSM, 0.2 μL of the bead solution was mixed with 40 μL of agarose gel which has a similar refractive index as that of water. The mixture was then introduced in a glass capillary, which was sealed and refrigerated for polymerization.

For X-ray CMT, 0.5 μL of the bead solution was mixed with 40 μL contrast agent and introduced in a capillary. The capillary was then refrigerated for polymerization of the contrast agent.

Image preprocessing

Image processing was carried out using Avizo® (FEI, Oregon, USA) 9 Fire Edition software.

Two-photon stacks were deconvolved using experimental red (for TAMRA) and green (for GFP) point spread functions (PSFs) obtained from imaging of fluorescent sub-resolution particles. The 'Deconvolution' function used an iterative maximum like-hood algorithm where the number of iterations (here 40) must be specified. The phantom stack, consisting of a red channel only, was deconvolved accordingly. The 0° and 90° biofilm stacks were manually registered and fused using the 'Add image' function which logically sums the image intensities.

Due to the difference between the refractive indices of glass and water, biofilm grown on the flow cell walls, in the laser direction, was difficult to observe. The custom designed caps and capillary holder illustrated in Figure 2

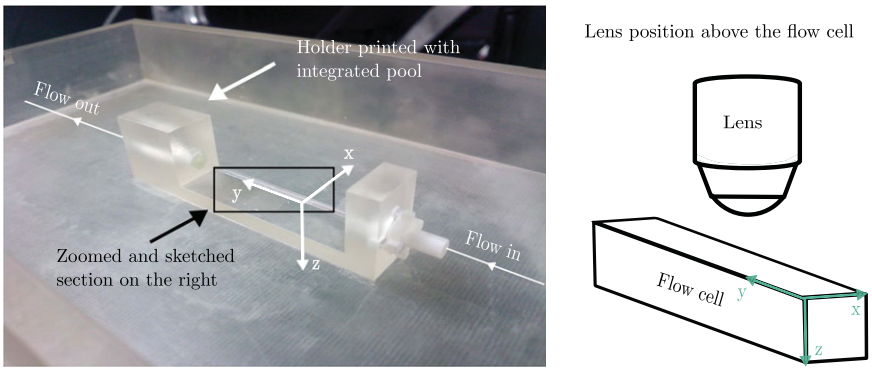

Fig. 2. Three-dimensional-printed flow cell (capillary) holder with silicone filled caps and integrated pool for immersion lens. The four notches enabled rotating the flow cell at four different angles. The picture was taken with the notches out, the cap well-fitted in the support which maintained the flow cell in place.

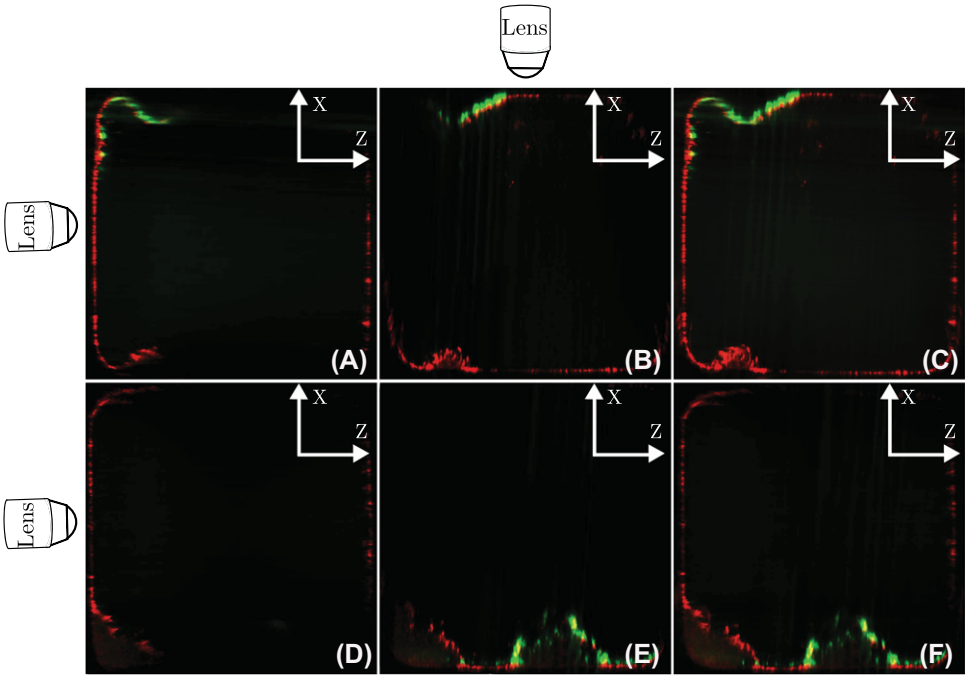

Fig. 3. From left to right: the image acquired with the flow cell positioned at 0° (A and D), then the image acquired with the flow cell rotated at 90° (B and E), where the complementary information on the biofilm grown on the top and bottom walls can be observed. At the far right (C and F) are the merged stacks of (A) and (B) and (D) and (E), respectively.

enabled rotating the capillary at two different angles (0° and 90°) to gather information on half of the flow cell's cross section. Figure 3 shows two-photon images of a *P. Aeruginosa* biofilm, where the position of the lens relative to the flow cell is shown to indicate the direction of acquisition. Figures 3(A) and (D) illustrate the images acquired with the flow cell positioned at 0° and Figures 3(B) and (E) show the images acquired with the flow cell rotated at 90° where the complementary information on the biofilm grown on the top and bottom walls can be observed. Finally, Figures 3(C) and (F) are the merged stacks of (A) and (B) and (D) and (E), respectivel.

The rotation of the capillary was seen to induce a shift of about 50 μm in the Y direction and about 100 μm in the Z direction for the corresponding image acquisitions. The 0° and 90° stacks thus had to be aligned before being merged. The stacks were then processed with a symmetric nearest neighbour filter which has the remarkable property of well preserving edges (Hall, 2007). This algorithm compares each voxel to its symmetrically opposite connected neighbours. The grey levels of these symmetric pairs of voxels, that are closest in intensity to the central one, are averaged. The centre voxel is then replaced by the mean of its current grey level and of this calculated average.

X-ray tomographic stacks were cropped to select only the part that was imaged by TPLSM. The stacks were then filtered using a non-local means filter. This algorithm looks for similar neighbourhoods, in a given search window, of the region around the current voxel (Buades *et al.*, 2005). It then computes the mean of all voxels in these neighbourhoods, weighted by how similar they are to the targeted one. This weighing function determining the similarity value is Gaussian. Under the assumption that the noise present in the image is white noise, this filter will preserve most features, even if they are small and thin.

Image segmentation

One way to proceed with segmentation for quantitative measurements is to optimize noise filtering as well as the different steps of binarization to obtain the best possible segmentation of the different phases. The main concern with this approach is that it fails to evaluate the uncertainty due to the fact that part of the information, primarily because of noise and artefacts, cannot be recovered. One way to tackle this issue is to further study the uncertainty propagation throughout the different steps and choices of parameters. However, such an analysis is difficult to perform. Here, we adopt a middle-ground approach: we hypothesize that the uncertainty can be bounded by using three completely different, simple and commonly used segmentation techniques (namely hysteresis, watershed and region growing). The first segmentation technique, hysteresis binarization, creates a binary image by specifying a lower and an upper threshold (Schlüter *et al.*, 2014). The voxels above the upper threshold and those above the lower threshold and below the upper one, that are connected to a voxel from the upper region, are selected. Watershed segmentation consists of viewing the grey-level image as a topographic map, with the brightness of each point being representative of its height (Wildenschild & Sheppard, 2013; Schlüter *et al.*, 2014). The map is then 'flooded' using an automatic gradient magnitude algorithm, creating barriers and basins corresponding to the grey levels. In region growing segmentation, a seed voxel is chosen and a grey-level range is specified. Then, all connected voxels, sharing at least one face (six possibilities for a voxel) with the chosen one and having a grey level from the specified range, are automatically selected, rendering the largest possible connected area within the user-specified range (Schlüter *et al.*, 2010). For the three segmentation methods, a binary image was obtained as final image.

Each approach required, at some step, a user-defined threshold. This value was chosen from the image histogram where it could be observed which range of grey levels belonged to a specific material. The impact of the choice of this threshold grey level was evaluated by segmenting using a value slightly above and below ($\pm 10\%$ of the grey-level range of the bead) the chosen one. The metrics obtained were then compared to the measurements obtained by the selected threshold.

Once all the images were segmented, automatic measurements were extracted from connected structures (using Avizo® 'Label analysis' function). For the beads, diameters in X, Y and Z direction obtained by the generated bounding box of each bead as well as surface area and volume (voxel count) were measured. From this volume, the diameter of an equivalent sphere was calculated and its discrepancy relative to the supplier's information and bright-field microscopy was determined. For the biofilm images, the maximum thickness was extracted along with volume and surface area. For thickness measurements, biofilm structures were isolated and the bounding box size in the dimension perpendicular to the flow cell walls was noted. The surface area was automatically estimated by the software from the boundary curve of the exposed outer voxel and in case of noncontinuous signal, chordal approximation was performed. The difference between X-ray CMT and TPLSM measurements was then determined and plotted.

Results

Bead phantom uncertainty analysis

Via TPLSM, the fluorescent micro-spheres were bright and uniformly distributed inside the capillary. The beads were highly radiopaque when imaged by X-ray CMT and appeared as small white spots. The sensitivity analysis for the choice of grey-level threshold rendered slightly larger (below threshold) or smaller (above threshold) beads, but the difference was inferior to the standard deviation obtained by the selected threshold. This indicated a very little impact of the operator's choice of grey level on the metrics. Figure 4 shows images of a microsphere obtained by TPLSM (right), at a spatial resolution of 1.186 μm/pixel and X-ray CMT (left), at 2 μm/pixel, where the background is greyish due to the contrast agent. Their respective grey-level histograms are illustrated on top and the result of three different binarization techniques below.

Measurements were performed for an average of 15 beads. Figure 5 shows the diameter measured in X, Y and Z directions using the segmentation techniques for both imaging modalities. The supplier's confidence interval (5.82 – 6.18 μm) is shown as well as the bright-field microscopy measurements (6.7 ± 0.05 μm).

Most measurements were between 6 and 7 μm, except for the Z direction of TPLSM because of the PSF. Indeed, this stretching of the fluorescence in the laser direction was due to the anisotropy intrinsic to the imaging approach and to the mismatch of refractive indices (water and glass) within the sample. The mean absolute error (relative to and normalized by 6 μm, i.e. supplier information) calculated for X-ray CMT for equivalent spherical diameter was 17.97% (see details in Table 1). For TPLSM, the mean absolute error was 14.79%. X-ray CMT slightly over-evaluated the phantom diameters, but the size of the error bars was similar in all three

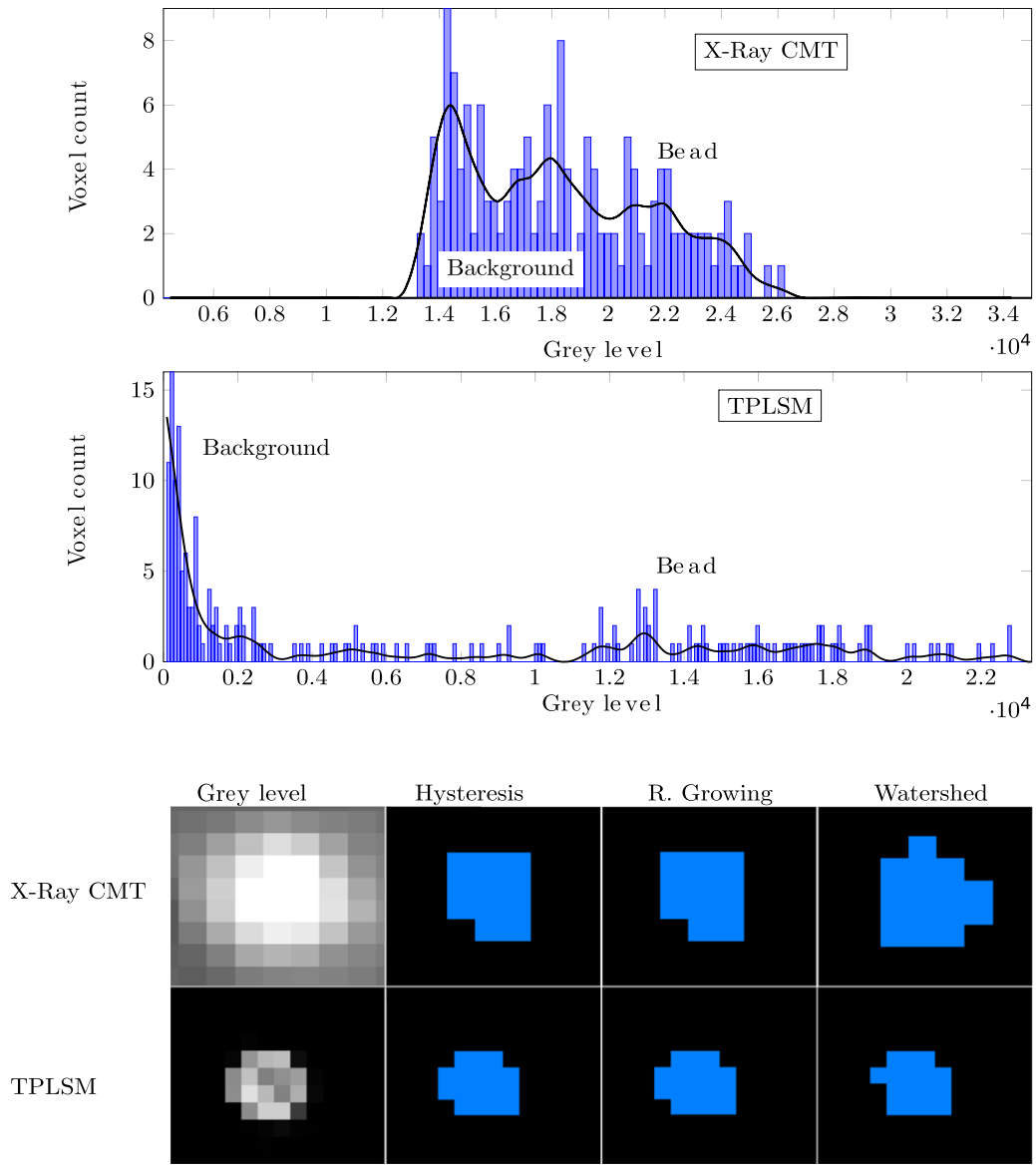

Fig. 4. Top and middle: grey-level histograms of a bead imaged by X-ray CMT and TPLSM, respectively. The smoothing spline (black) illustrates the main peaks. For X-ray CMT, the first two left peaks belong to the greyish background, the last one represents the bead. For TPLSM, the left peak belongs to the black background and the small centre peak represents the bead. Bottom: grey-level images of a bead via X-ray CMT and TPLSM along with the results of the three segmentation techniques, namely hysteresis, region growing and watershed. TPLSM spatial resolution was 1.186 μm/pixel (5 pixels $\sim$ 6 μm) and X-ray CMT was 2 μm/pixel (3 pixels = 6 μm).

directions showing the isotropic property of this modality and indicating a smaller variability. This overestimation may be due to perhaps inexact supplier information, since bright-field microscopy measurements gave a relatively larger diameter (6.7 μm), thus reducing the error generated by X-ray CMT. In Table 1, the absolute error (relative to and normalized by 6 and 6.7 μm), on equivalent spherical diameter for the two imaging modalities and three image segmentation techniques, is illustrated. It can be indeed observed that the error generated by the two modalities was greatly decreased when compared with bright-field microscopy.

The mean absolute errors normalized by supplier's information and bright-field microscopy, respectively, for surface area and volume of TPLSM and X-ray CMT are shown in Table 2. It can be noted that for surface area measurements, X-ray CMT proved more precise (11.62% compared to 28.9% for TPLSM). For volume, on contrary, TPLSM was more accurate. For both metrics, the error bars of both imaging modalities were of

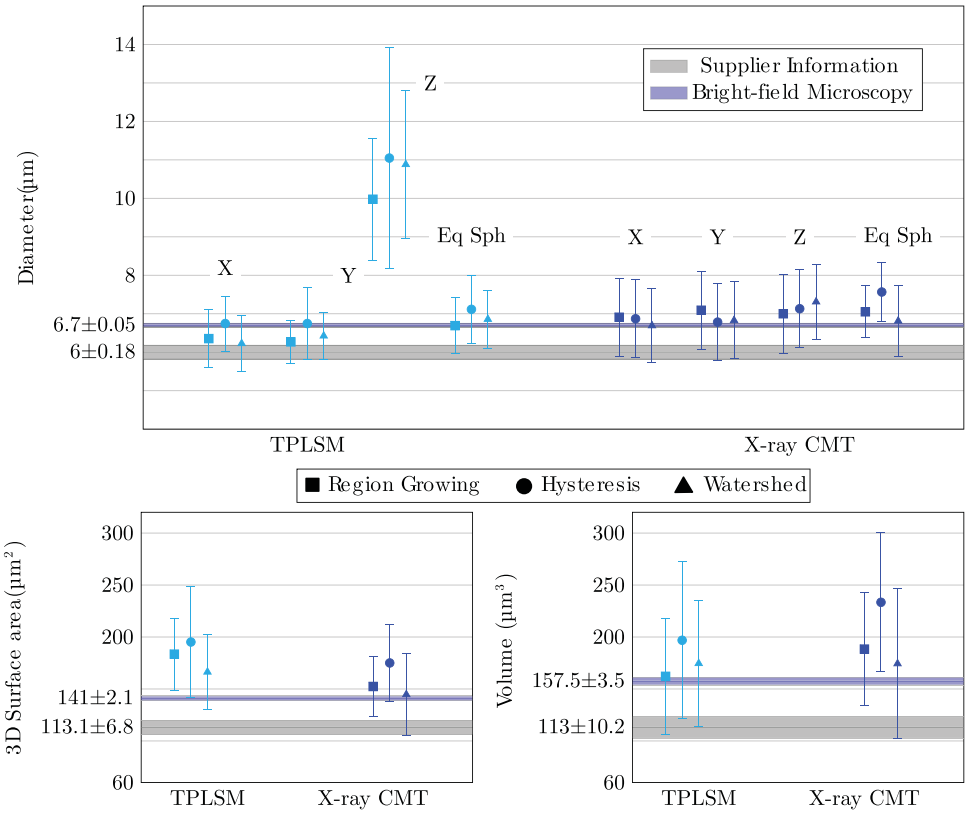

Fig. 5. Top: mean phantom diameter determined in X, Y and Z directions and equivalent spherical diameter derived from 3D volumes, the error bars representing the standard deviation. Measurements were made by processing the same beads with different segmentation techniques, namely region growing, watershed and hysteresis. Bottom: mean surface area (left) and mean volume (right) are illustrated. For all plots, the control dimensions (supplier information and bright-field microscopy) are also illustrated.

Table 1. Absolute error, relative and normalized by 6 μm (supplier's information) and 6.7 μm (bright-field microscopy), for TPLSM and X-ray CMT and using the three segmentation techniques (region growing, hysteresis and watershed).

Control diameter	Imaging modality	Region growing	Hysteresis	Watershed	Mean error
Supplier's information (6 μm)	TPLSM	11.52%	18.58%	14.28%	14.79%
	X-ray CMT	17.51%	26.08%	13.54%	17.97%
Bright-field microscopy (6.7 μm)	TPLSM	0.13%	6.19%	2.34%	2.89%
	X-ray CMT	5.24%	12.91%	1.68%	6.61%

comparable order of magnitude. In any case, X-ray CMT imaging was slightly less precise than TPLSM for phantom imaging in this set up, except for surface area metrics and watershed segmentation for diameter measurements.

Comparison of TPLSM and X-ray CMT acquisitions of biofilm images

Visual comparison between TPLSM (red and green) images overlaid with X-ray CMT (grey) stacks (Fig. 6) shows biofilm structures on the flow cell wall. Two samples are illustrated (upper and lower images) and the orthogonal views [XZ for (A) and (D), XY for (B) and (E) and YZ for (C) and (F)] of each are shown. Some barium sulphate aggregates can be observed as very bright spots, immobilized by the polymerization of the gel and thus confirming the sedimentation issue resolution. The white dashed rectangles represent the portion of the flow cell where maximum two-photon signal was obtained (using two angles of acquisition) for quantitative analysis.

For TPLSM, biofilm structures being more than 50 μm in depth appeared hollow. This is because the fluorescence signal was blocked by the biofilm layer closest to the lens. This phenomenon also shielded successive biofilm formations in the laser direction as shown in Figure 3(D)–(F), where only one

Table 2. Absolute error, relative and normalized by supplier's information and bright-field microscopy for 3D metrics (surface area and volume) of TPLSM and X-ray CMT imaged beads.

Measurement	Control metrics	Imaging modality	Mean error
Surface area	Supplier's information ($113\ \mu m^2$)	TPLSM	60.8%
		X-ray CMT	39.3%
	Bright-field microscopy ($141\ \mu m^2$)	TPLSM	28.9%
		X-ray CMT	11.62%
Volume	Supplier's information ($113\ \mu m^3$)	TPLSM	57%
		X-ray CMT	75.8%
	Bright-field microscopy ($157\ \mu m^3$)	TPLSM	13.3%
		X-ray CMT	26.6%

biofilm structure appeared when imaging at 0°. The appearing void structures are pointed by the white arrows, where it can be seen that only the contour of the biofilm formation could be visualized. The fact that these structures came out as hollow leads to unreliable calculation of biofilm volume by the segmentation techniques (Fig. 7). A correction was achieved when the structure's contour was well-enough delineated, where the void part was filled manually. This corrected TPLSM stack was labelled with a star*. In some structures (see cyan arrows in Fig. 6D), it was not possible to properly reconstruct the whole contour as there was missing signal, only thickness and surface area measurements were performed then. The plots in Figure 7 illustrate the quantitative analysis for distinct samples (in different colours), each shape representing a segmentation technique. Four biofilm structures noted by S1S1, S1S2, S2S1 and S2S2 (two from each sample) are illustrated. They correspond to a region of interest in the vicinity of the biofilm structures pointed by arrows in Figure 6.

Volume measurements using X-ray CMT captured more biofilm than TPLSM, even when the hollow structures were manually filled. This procedure for correcting the fluorescence shielding was minimal so as not to introduce unwanted excess signal and may explain this difference (especially for the S1S2 in cyan). In average, TPLSM found 0.71 times less biofilm than X-ray CMT and TPLSM* found 0.28 times less. Also, X-ray CMT showed more variability among the segmentation techniques than TPLSM. For 3D surface area, TPLSM generally had larger values than X-ray CMT, possibly because of the higher resolved images, showing more tortuous details. There is an exception for S1S2 (cyan) as TPLSM showed less signal for the thin biofilm layer next to the main structure (see Fig. 6A lower part). When the surfaces were large, for instance for S1S1 (blue) and S1S2 (cyan), watershed binarization led to smaller values. As this segmentation technique tends to smooth the images with its gradient magnitude algorithm, it possibly removed details of biofilm structure, decreasing exposed surface area. Concerning thickness measurements,

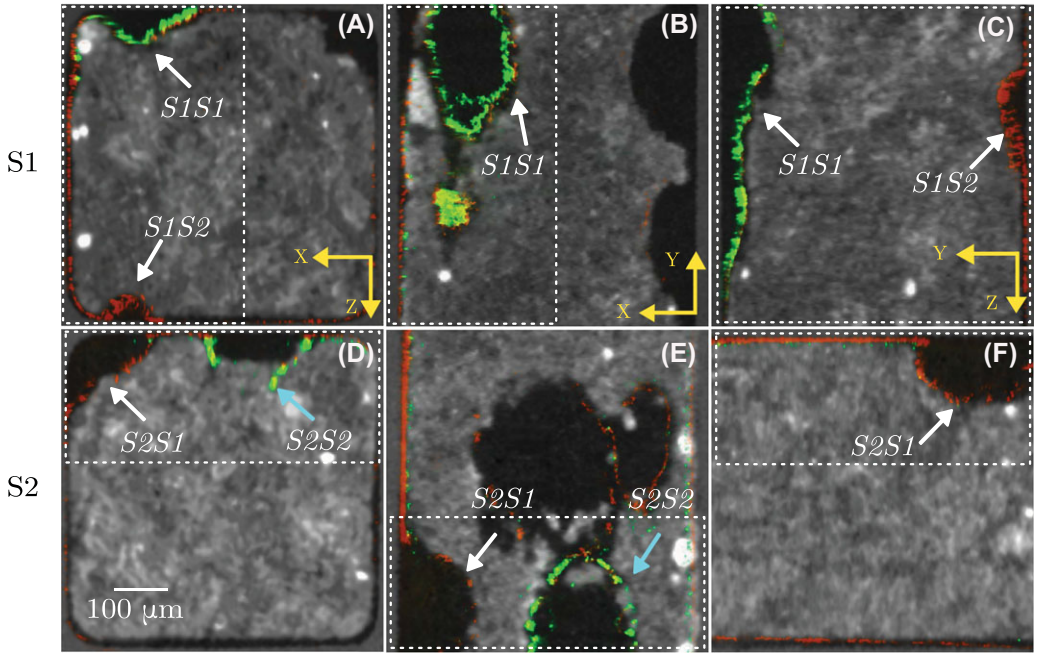

Fig. 6. Visual comparison of TPLSM images superimposed on X-ray CMT stacks for two samples (S1 upper and S2 lower). (A) and (D) illustrate the cross section of the flow cell (XZ) for two different samples, (B) and (E) and (C) and (F) show the side views XY and YZ, respectively. White dashed rectangles represent the portion of the flow cell used for quantitative analysis, the arrows show TPLSM structures appearing hollow, in white when manual correction was possible and in cyan, when the contour of the structure was not well delineated enough. Fluorescence was enhanced for visual purposes.

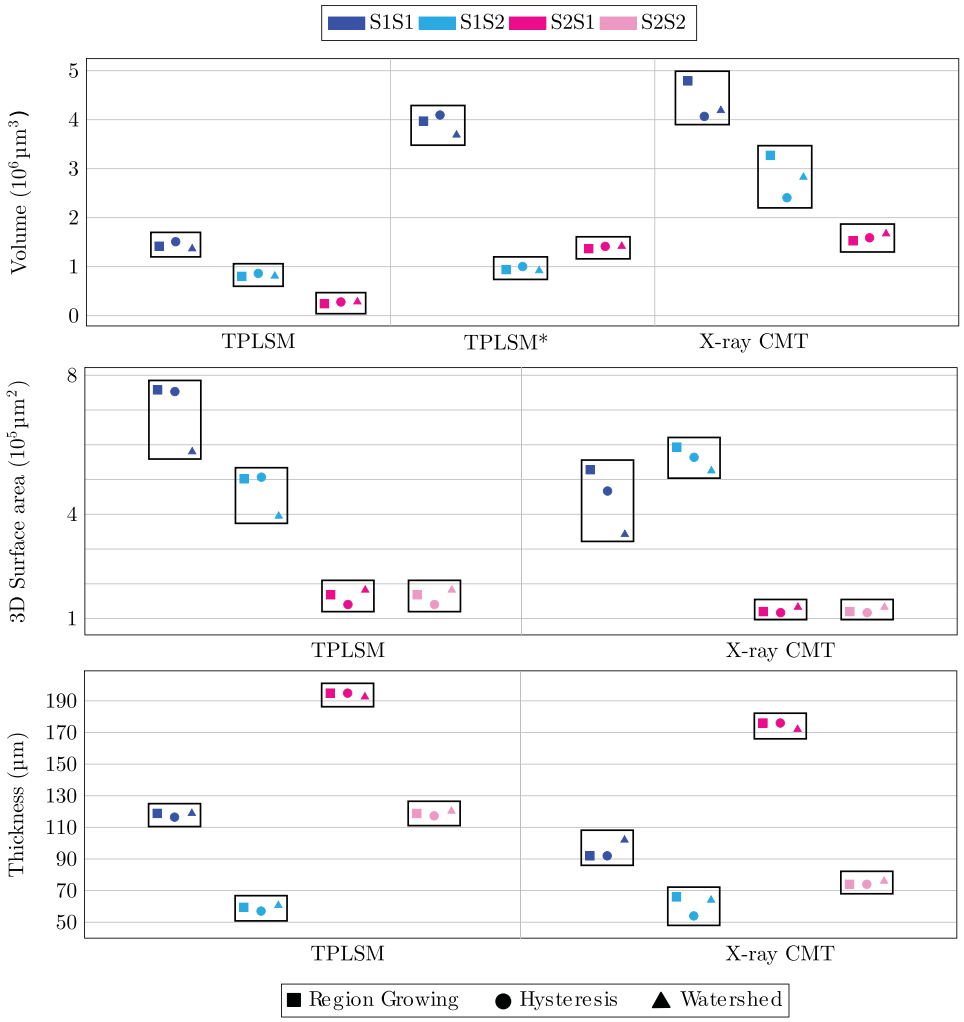

Fig. 7. Quantitative analysis of biofilm metrics: comparison between both imaging modalities where each colour represents a sample and the three used segmentation techniques are illustrated by different shapes. Volume measurements are displayed in the upper plot where TPLSM* represents the corrected hollow structures. Three-dimensional surface areas are shown in middle plot and maximum thickness in lower plot.

the difference between the means for each structure was 44.14 μm (pink), 22.71 μm (blue), 19.44 μm (magenta) and 2.31 μm (cyan). In average, TPLSM found 0.18 times thicker biofilms than X-ray CMT.

The correspondence between both imaging modalities seems to depend on the type of biofilm structure that is imaged. For simple, relatively flat structures, we observe that the two images have almost perfect correspondence (see Fig. 6A and C on the right wall). However, thicker structures appear hollow via TPLSM, whereas X-ray CMT renders them as slightly flattened (see Fig. 6C left wall and D middle structure). The thickness measurements confirm this observation as for big structures, the difference in the means is larger (22.71 and 44.14 μm, respectively), whereas it is 2.31 μm for a small structure. For S2S1 (magenta), which is the biofilm formation situated in the flow cell corner (Fig. 6D), there is little difference in thickness (TPLSM finds 0.1 times more than X-ray CMT) probably because this cornered-type structure had a larger adhesion surface increasing its stability and reducing its exposition to flow-induced shear stress.

Figure 8 illustrates the 3D images of both sample images by TPLSM (right) and X-ray CMT (left). The four analysed structures are pointed by the black arrows. The two image modalities show corresponding 3D biofilm formation with very good similarity. It can be observed that X-ray CMT yielded smoother images than TPLSM, probably due to its coarser spatial resolution, also, the 'flattening' effect of X-ray CMT on the structures from S1 can be assessed. Discrepancies in the presence of biofilm at certain locations can also be observed between the two image modalities (see Supplementary Fig. S1 for superimposed 3D figures of both imaging techniques). For example, in S1, there is thicker biofilm on the upper flow cell wall via X-ray CMT than TPLSM, and oppositely, less biofilm on the lower flow cell wall. The same applies to S2,

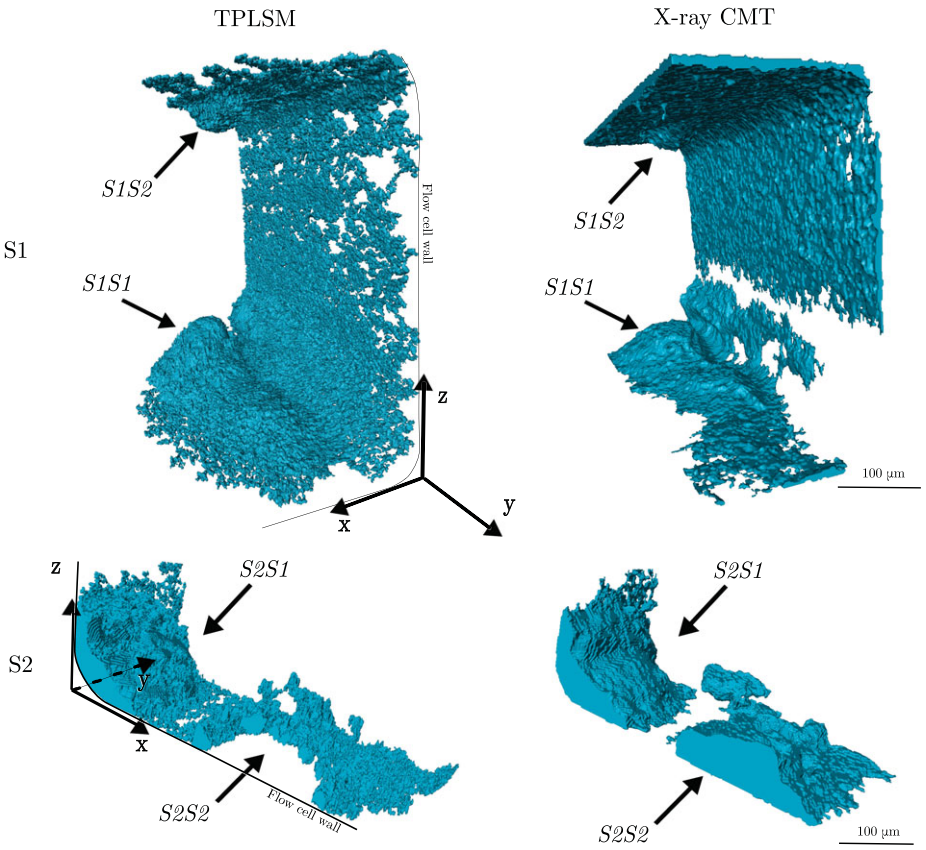

Fig. 8. Three-dimensional visualizations of the analysed samples showing corresponding biofilm formation on the flow cell wall. The different structures pointed by arrows are recognizable.

where there seems to be more biofilm captured by TPLSM than X-ray CMT on the flow cell wall. In these TPLSM 3D images, hollow structures having a well-delineated contour have been manually filled. There is an exception for S2S1 where there was not sufficient signal and the structure thus still appears void.

Discussion

Although the setup was optimized for TPLSM in capillary tubes, X-ray CMT proved quite precise in characterizing the phantom geometry. TPLSM is very accurate in the focal plane (X and Y directions) but has poor accuracy in the Z direction (Fig. 5). This is due to the anisotropy intrinsic to the imaging approach and to the mismatch of refractive indices, which produces large PSFs, which stretch the fluorescence signal in the Z direction, even after deconvolution with experimental PSF acquired under biofilm imaging parameters. Other microscopy configurations could have been used for single phantom (micro-sphere) imaging, increasing the accuracy and easing the deconvolution. However, such parameters would have been irrelevant for biofilm imaging, highlighting the difficulty in accurately using TPLSM for imaging large volumes. Even though it slightly overestimates phantom diameters, X-ray CMT provides isotropic resolution (voxel size of 2 μm here) and an error of about 17% compared to supplier information, whereas the error using TPLSM was about 14% but with anisotropic spatial resolution. The bright-field microscopy measurements indicate a possible erroneous supplier information for the phantom geometry, and thus greatly reducing the error generated by our protocol using X-ray CMT (6.61%). Other sources of uncertainty are the large micro-sphere versus fluid absorption contrast, potential biases from the segmentation techniques and artefacts intrinsic to X-ray CMT such as beam hardening. Such errors could be corrected by working with more resolved systems, using synchrotron radiation or improving the image processing. Using less X-ray absorbent micro-spheres could also improve this analysis.

The situation is a lot more complicated when comparing both methods for biofilm imaging. Qualitatively, a very good correspondence between X-ray CMT and TPLSM images is observed (see Fig. 6 and the 3D volumes in Fig. 8), with a good correlation showing contrast in CMT and fluorescence in TPLSM. The correspondence between both modalities also seems to depend on the type of biofilm structures that are being visualized. For relatively flat structures, the two images have almost perfect correspondence (Fig. 6A). However, for thicker

biofilm structures larger than about 50 μm, TPLSM images show hollow biofilm formations, this being a consequence of fluorescence shielding and a major issue of the method for imaging large biofilm structures.

For larger structures, X-ray CMT also provides slightly flattened structures (Fig. 6B). We hypothesize that this 'flattening' effect results from the multiple stresses the biofilm was subjected to. Part of it is most likely due to the first acquisitions by TPLSM. Indeed, the laser excitation is mostly infrared and water (being highly absorbent) inside the sample tends to heat. Even if flow was maintained during image acquisition to minimize this warming effect, such heating probably had an impact on the biofilm structures. Even if all precautions were taken to decrease the duration of image acquisition (less time on each slice and less averaging), in many samples it could be visually observed that the flow cell contained slightly less biofilm after the TPLSM imaging, just before introduction of the contrast agent for X-ray CMT. Another important factor involves mechanical interactions between the contrast agent and the biofilm, including abrasion and shear stress upon introduction and the polymerization of the gel (e.g. swelling) that could flatten the biofilm. The concentration of 2% (w/v) gel was carefully chosen to be minimal for a complete polymerization, but biofilm damage, especially for thick and weakened structures, cannot be fully excluded. Still, our protocol for injection has been meticulously devised and every detail is of relative importance for an optimized contrast agent introduction.

However, contrary to Carrel *et al.* (2017), we did not observe, either with naked eye or by comparison of both modalities, that introducing the contrast agent leads to massive sloughing of biofilms. There are different reasons why this might be the case. First and foremost, Carrel *et al.* (2017) mentioned the introduction of air bubbles in their column during injection of barium sulphate; we believe that this fourth phase could have interacted and damaged biofilm structures as we have observed air bubbles tearing biofilm in capillaries during early experiments. It is also important to note that their sample had already been irradiated once before the introduction of barium sulphate. X-rays can have a harmful impact (Hitchcock *et al.*, 2005; Iltis *et al.*, 2011) on both the micro-organisms and the extracellular polymeric substances (EPSs), this could have weakened the biofilm structures and increased abrasion effects. Other reasons for these discrepancies can be attributed to the difference in the flow rate. The Darcy velocity in Carrel *et al.* (2017) was 1.06 mm/s, whereas the velocity for our flow cell was 52 mm/s. This increase in Darcy velocity could have generated more resistant biofilm structures that can sustain greater shear stress. In addition, the bacterial strain we used, *P. Aeruginosa*, is known to produce strong biofilms (Ma *et al.*, 2009; Lieleg *et al.*, 2011), whereas their team grew biofilms from unknown possibly multiple micro-organisms. Another aspect is the decreased viscosity of our contrast agent along with the low injection flow rate which, we believe, induced less shear stress upon the biofilm structures.

Conclusion

Qualitative and quantitative 3D analysis showed that the proposed contrast agent enables a reliable observation of biofilm using X-ray CMT. We have quantified the uncertainty yielded by our protocol and showed the importance of such analysis if any metrics are to be extracted from the images. Also, for a fixed imaging modality and sample, the metrics obtained were nearly independent of the binarization process, confirming the quality of our imaging acquisitions. The poor correspondence for some measurements showed the potential damage imaging that techniques can have on delicate biofilm structures, especially TPLSM heating effect on water. Our protocol has also revealed advantages of X-ray CMT over TPLSM for 3D imaging, notably for large volumes, with a very good isotropic spatial resolution of 2 μm/pixel and the absence of optical shielding artefacts. Our method is robust, reproducible and reliable for strong biofilm structures of *P. Aeruginosa* grown at a constant flow rate. As the very first comparison with the most widely used technique in the field and uncertainty analysis made for imaging of biofilm using X-ray CMT, it is very encouraging and provides an efficient contrast agent for future studies in porous media. Experimenting other bacterial strains at different flow rates will evaluate the range of applicability of our protocol. Other perspectives are the investigation of the impact of other parameters such as flow rate, nutrient concentration and pore geometry on the morphology and the distribution of *P. Aeruginosa* biofilms in porous media of pore size larger than 100 μm.

Acknowledgements

We thank Ruddy Soeparno and Maëlle Ogier from IMFT for their help and Sophie Allart, Magda Rodrigues and Astrid Canivet for their assistance at the imaging facility platform of the Centre de Physiopathologie de Toulouse Purpan (INSERM).

This project was funded by the grant BioPorousLab (Transversalité, 2014) from the IDEX UNITI.

The authors declare no conflict of interest.

References

Armstrong, R.T. & Wildenschild, D. (2012) Microbial enhanced oil recovery in fractional-wet systems: a pore-scale investigation. *Transp. Porous Media* **92**(3), 819–835.

Buades, A., Coll, B. & Morel, J.M. (2005) A non-local algorithm for image denoising. In *2005 IEEE Computer Society Conference on Computer Vision and Pattern Recognition (CVPR'05)*. Vol. 2, pp. 60–65.

Carrel, M., Beltran, M.A., Morales, V.L., Derlon, N., Morgenroth, E., Kaufmann, R. & Holzner, M. (2017) Biofilm imaging in porous media by laboratory X-ray tomography: combining a non-destructive contrast agent with propagation-based phase-contrast imaging tools. *PLoS One* **12**(7), 1–18.

Choi, O., Yu, C.-P., Fernández, G.E. & Hu, Z. (2010) Interactions of nanosilver with *Escherichia coli* cells in planktonic and biofilm cultures. *Water Res.* **44**(20), 6095–6103.

Cunningham, A.B., Characklis, W.G., Abedeen, F. & Crawford, D. (1991) Influence of biofilm accumulation on porous media hydrodynamics. *Env. Sci. Technol.* **25**(7), 1305–1311.

Davit, Y., Iltis, G., Debenest, G., Veran-Tissoires, S., Wildenschild, D., Gerino, M. & Quintard, M. (2011) Imaging biofilm in porous media using X-ray computed microtomography. *J. Microsc.* **242**(1), 15–25.

Fierer, N. & Jackson, R.B. (2006) The diversity and biogeography of soil bacterial communities. *Proc. Natl. Acad. Sci. U. S. A.* **103**(3), 626–631.

Hall, M. (2007) Smooth operator: smoothing seismic interpretations and attributes. *Leading Edge* **26**(1), 16–20.

Hall-Stoodley, L., Costerton, J.W. & Stoodley, P. (2004) Bacterial biofilms: from the natural environment to infectious diseases. *Nat. Rev. Microbiol.* **2**(2), 95–108.

Hitchcock, A.P., Morin, C., Zhang, X., *et al.* (2005) Soft X-ray spectromicroscopy of biological and synthetic polymer systems. *J. Electron Spectrosc. Relat. Phenomena* **144**, 259–269. In *Proceeding of the 14th International Conference on Vacuum Ultraviolet Radiation Physics*.

Ho, K.-L., Chung, Y.-C., Lin, Y.-H. & Tseng, C.-P. (2008) Microbial populations analysis and field application of biofilter for the removal of volatile-sulfur compounds from swine wastewater treatment system. *J. Hazard. Mater.* **152**(2), 580–588.

Iltis, G.C., Armstrong, R.T., Jansik, D.P., Wood, B.D. & Wildenschild, D. (2011) Imaging biofilm architecture within porous media using synchrotron-based X-ray computed microtomography. *Water Resour. Res.* **47**(2), W02601.

Kim, J.-W., Choi, H. & Pachepsky, Y.A. (2010) Biofilm morphology as related to the porous media clogging. *Water Res.* **44**(4), 1193–1201.

Leis, A.P., Schlicher, S., Franke, H. & Strathmann, M. (2005) Optically transparent porous medium for nondestructive studies of microbial biofilm architecture and transport dynamics. *Appl. Env. Microbiol.* **71**(8), 4801–4808.

Leon-Morales, C., Leis, A.P., Strathmann, M. & Flemming, H.-C. (2004) Interactions between laponite and microbial biofilms in porous media: implications for colloid transport and biofilm stability. *Water Res.* **38**(16), 3614–3626.

Lewandowski, Z. & Beyenal, H. (2014) *Fundamentals of Biofilm Research*. 2nd edn. CRC Press Taylor and Francis Group, UK.

Lieleg, O., Caldara, M., Baumgartel, R. & Ribbeck, K. (2011) Mechanical robustness of *Pseudomonasaeruginosa* biofilms. *Soft Matter* **7**, 3307–3314.

Ma, L., Conover, M., Lu, H., Parsek, M.R., Bayles, K. & Wozniak, D.J. (2009) Assembly and development of the *Pseudomonas aeruginosa* biofilm matrix. *PLoS Pathog.* **5**(3), 1–11.

Mah, T.-F.C. & O'Toole, G.A. (2001) Mechanisms of biofilm resistance to antimicrobial agents. *Trends Microbiol.* **9**(1), 34–39.

Mitchell, A.C., Phillips, A.J., Hiebert, R., Gerlach, R., Spangler, L.H. & Cunningham, A.B. (2009) Biofilm enhanced geologic sequestration of supercritical CO2. *Int. J. Greenhouse Gas Control* **3**(1), 90–99.

Morozova, D., Zettlitzer, M., Let, D. & Würdemann, H. (2011) Monitoring of the microbial community composition in deep subsurface saline aquifers during CO2 storage in Ketzin, Germany. *Energy Procedia* **4**, 4362–4370. In *10th International Conference on Greenhouse Gas Control Technologies*.

Neu, T.R. & Lawrence, J.R. (2015) Innovative techniques, sensors, and approaches for imaging biofilms at different scales. *Trends Microbiol.* **23**(4), 233–242.

Rittmann, B., Sharp, R., Cunningham, A., Komlos, J. & Billmayer, J. (1999) Microbial ecology of biofilms observation of thick biofilm accumulation and structure in porous media and corresponding hydrodynamic and mass transfer effects. *Water Sci. Technol.* **39**(7), 195–201.

Rolland du Roscoat, S., Martins, J.M., Séchet, P., Vince, E., Latil, P. & Geindreau, C. (2014) Application of synchrotron X-ray microtomography for visualizing bacterial biofilms 3D microstructure in porous media. *Biotechnol. Bioeng.* **111**(6), 1265–1271.

Schlüter, S., Sheppard, A., Brown, K. & Wildenschild, D. (2014) Image processing of multiphase images obtained via X-ray microtomography: a review. *Water Resourc. Res.* **50**(4), 3615–3639.

Schlüter, S., Weller, U. & Vogel, H.-J. (2010) Segmentation of X-ray microtomography images of soil using gradient masks. *Comp. Geosci.* **36**(10), 1246–1251.

Seymour, J.D., Codd, S.L., Gjersing, E.L. & Stewart, P.S. (2004) Magnetic resonance microscopy of biofilm structure and impact on transport in a capillary bioreactor. *J. Magn. Reson.* **167**(2), 322–327.

Singh, R., Paul, D. & Jain, R.K. (2006) Biofilms: implications in bioremediation. *Trends Microbiol.* **14**(9), 389–397.

Stewart, P.S. & Costerton, J.W. (2001) Antibiotic resistance of bacteria in biofilms. *Lancet* **358**(9276), 135–138.

Stoodley, P.E.A. (2011) Orthopaedic biofilm infections. *Curr. Orthop. Pract.*

Sugimoto, S., Okuda, K.-I., Miyakawa, R., *et al.* (2016) Imaging of bacterial multicellular behaviour in biofilms in liquid by atmospheric scanning electron microscopy. *Sci. Rep.* **6**, 25889.

Thullner, M. & Baveye, P. (2008) Computational pore network modeling of the influence of biofilm permeability on bioclogging in porous media. *Biotechnol. Bioeng.* **99**(6), 1337–1351.

Vafai, K., editor (2010) *Porous Media: Applications in Biological Systems and Biotechnology*. Taylor & Francis Group, LLC.

Valiei, A., Kumar, A., Mukherjee, P.P., Liu, Y. & Thundat, T. (2012) A web of streamers: biofilm formation in a porous microfluidic device. *Lab Chip* **12**, 5133–5137.

Valls, M. & de Lorenzo, V. (2002) Exploiting the genetic and biochemical capacities of bacteria for the remediation of heavy metal pollution. *FEMS Microbiol. Rev.* **26**(4), 327.

Vroom, J.M., De Grauw, K.J., Gerritsen, H.C., Bradshaw, D.J., Marsh, P.D., Watson, G.K., Birmingham, J.J. & Allison, C. (1999) Depth penetration and detection of pH gradients in biofilms by two-photon excitation microscopy. *Appl. Env. Microbiol.* **65**(8), 3502–3511.

Wildenschild, D. & Sheppard, A.P. (2013) X-ray imaging and analysis techniques for quantifying pore-scale structure and processes in subsurface porous medium systems. *Adv. Water Resourc.* **51**, 217–246. 35th Year Anniversary Issue.

Yarwood, R.R., Rockhold, M.L., Niemet, M.R., Selker, J.S. & Bottomley, P.J. (2002) Noninvasive quantitative measurement of bacterial growth in porous media under unsaturated-flow conditions. *Appl. Env. Microbiol.* **68**(7), 3597–3605.

Supporting Information

Additional supporting information may be found online in the Supporting Information section at the end of the article.

Fig. S1. Three-dimensional superimposed visualizations of the analysed samples showing the discrepancies yielded by X-ray CMT (green) and TPLSM (blue) images.